Research article

Terpene Scaffolds as Allosteric Inhibitors of PTP1B: An Integrated Docking, MD, and MM/PBSA Study

Naif Ghazi Altoom ¹

¹ Department of Biology, King Khalid Military Academy, P.O. Box 22140, Riyadh 11495, Saudi Arabia

RECEIVED 25 September 2025 REVISED 22 October 2025 ACCEPTED 30 October 2025 ONLINE 6 November 2025

CITATION

Altoom N. G. (2025). Terpene Scaffolds as Allosteric Inhibitors of PTP1B: An Integrated Docking, MD, and MM/PBSA Study. Spectrum Science Journal, 2(1): 22-33

DOI:10.21608/sasj.2025.431167.1010

CORRESPONDENCE

Naif Ghazi Altoom Email: <u>Alotaibin@kkma.edu.sa</u>

The Scientific Association for Studies and Applied Research (SASAR) https://sasj.journals.ekb.eg



COPYRIGHT

©2025 by the authors. Submitted for possible open access publication under the terms and conditions of the Creative Commons Attribution (<u>CC</u> BY) license.

Spectrum Science Journal PRINT ISSN: 3062-5068 ONLINE ISSN: 3062-5076

Abstract:

Protein tyrosine phosphatase 1B (PTP1B) is a validated antidiabetic and anti-obesity target whose activity can be attenuated by small molecules engaging an allosteric cleft between helices α3/α7 beneath the Phe196/Phe280 "aromatic clamp." Motivated by the tractability of terpene scaffolds, we evaluated artemisinic acid, dehydroabietic acid, and santonin as PTP1B allosteric inhibitors using an integrated in-silico pipeline. The 1T49 crystal structure was prepared and used for structure-based docking, followed by 200-ns explicit-solvent molecular dynamics (MD) and MM/PBSA end-point free-energy analysis. Docking located all three ligands in the $\alpha 3/\alpha 7$ pocket with predicted affinities of -7.6 (artemisinic acid), -8.1 (dehydroabietic acid), and -8.7 kcal·mol⁻¹ (santonin), reproducing the characteristic hydrophobic contacts to Phe196/Phe280 and polar interactions at the mouth (Asn193/Lys197/Glu200). MD indicated stable protein backbones for all complexes, while ligand mobility differentiated the series: the dehydroabietic-acid complex showed the lowest ligand RMSD and most persistent mouth hydrogen bonding; artemisinic acid was intermediate; santonin displayed greater early pose wandering despite favorable docking. MM/PBSA ranked dehydroabietic acid as the most favorable binder, followed by artemisinic acid, with santonin weakest—consistent with stronger van-der-Waals/packing and a smaller desolvation penalty for the abietane scaffold. Collectively, the data highlight deep hydrophobic burial against the aromatic clamp, plus one to two mouth-region polar contacts, as the key determinants of allosteric stabilization. Dehydroabietic acid emerges as a promising lead for optimization, with clear vectors to enhance potency while maintaining pocket complementarity. These findings support terpene-derived chemotypes as credible starting points for selective PTP1B allosteric inhibitor design.

Keywords: PTP1B; allosteric inhibition; terpenes; dehydroabietic acid; artemisinic acid; santonin; molecular docking; molecular dynamics; MM/PBSA.

Introduction

Protein tyrosine phosphatase 1B (PTP1B) is a key negative regulator of insulin and leptin signaling that dephosphorylates the insulin receptor and IRS proteins, thereby dampening downstream pathways linked to glucose homeostasis and energy balance [1]. Its dysregulation has been associated with insulin resistance, obesity, and related metabolic disorders, making PTP1B a validated enzyme target in antidiabetic drug discovery [2]. In vitro, PTP1B activity is routinely quantified using colorimetric or fluorometric phosphatase assays (e.g., p-nitrophenyl phosphate, pNPP), enabling the ranking of small-molecule inhibitors and natural products by potency and selectivity [3].

Recent reviews also highlight multiple intervention modes (orthosteric, allosteric, and bidentate inhibition), underscoring both the promise and selectivity challenges of this class [4].

Natural terpenes remain a prolific source of PTP1B-modulating chemotypes [5]. Surveys of natural products report hundreds of PTP1B inhibitors spanning terpenoid scaffolds, and abietane-type diterpenoids in particular have shown tractable, tunable inhibition with clear structure—activity relationships around the carboxylate-bearing ring system [6]. Against this backdrop, we selected three readily available and structurally diverse terpenes (Figure 1)—artemisinic acid (a sesquiterpene carboxylic acid and biosynthetic precursor to artemisinin), dehydroabietic acid (an abietane resin acid), and santonin (a classic sesquiterpene lactone)—as representatives to probe PTP1B inhibition [7-9]. Abietane frameworks (e.g., abietic/dehydroabietic acid analogs) have been validated biochemically against PTP1B and optimized through derivatization of the C-18 carboxylate; sesquiterpene lactones are broadly bioactive and have been mined for metabolic-relevant enzyme modulation; and Artemisia-derived metabolites and precursors have repeatedly yielded PTP1B-active constituents, motivating evaluation of artemisinic acid itself as a simple, drug-like probe [10].

Figure 1. Chemical structures of studied terpenes.

Complementing wet-lab assays with in silico techniques can de-risk and accelerate hit triage by revealing binding modes, stability, and relative affinities in the enzyme environment [11]. Rigid- and induced-fit docking rapidly generate plausible PTP1B-ligand poses and qualitative rank-ordering; explicit-solvent molecular dynamics (MD) tests pose persistence and loop conformational effects (e.g., the catalytically essential WPD loop in PTP1B); and end-point free-energy methods such as MM/PBSA provide efficient, physics-based estimates that correlate with experimental trends when applied carefully [12, 13]. Consensus pipelines that couple docking, MD, and MM/PBSA have been shown to enrich true actives across enzyme targets and to rationalize SAR, making them well suited to prioritize terpene analogs before synthesis or purchase [14-16].

Accordingly, this study aims (i) to evaluate the in vitro inhibitory activity of artemisinic acid, dehydroabietic acid, and santonin against human PTP1B; (ii) to rationalize their binding using structure-based docking and MD; and (iii) to estimate relative binding free energies via MM/PBSA, thereby guiding future optimization of terpene-derived PTP1B inhibitors.

Materials and Methods

System preparation

The three-dimensional coordinates of human PTP1B were retrieved from the Protein Data Bank (PDB ID: 1T49), a structure solved with an allosteric ligand and widely used to model the $\alpha 3/\alpha 7$ pocket near Phe196/Phe280 [17]. The protein was curated in PyMOL (v2.5+) by stripping crystallographic waters and the co-crystallized ligand, then adding hydrogens and assigning physiological protonation states to prepare a clean receptor for structure-based work. Geometry refinement of the apo enzyme was carried out in GROMACS (2022.4) using the CHARMM36m all-atom protein force field to relieve clashes and optimize local stereochemistry prior to docking and dynamics [18].

Ligands were built in UCSF Chimera, stereochemistry verified and saved as PDB files. Their gasphase geometries were then optimized with density-functional theory (B3LYP/6-311G(d,p)) in Gaussian 16 to obtain well-relaxed conformers for docking [19-22]. Consistent with reported PTP1B work on small natural products, this preparation targets the allosteric binding environment characterized in 1T49 and later exploited in his coumarin/phenolic studies.

Molecular docking

Docking was performed with AutoDockTools 1.5.7 and AutoDock Vina [23, 24]. Receptor and ligands were converted to PDBQT; the search space was centered on the allosteric pocket (approx. x=55.92, y=29.81, z=21.65) with a $34\times34\times34$ Å grid and default spacing (0.375 Å). Exhaustiveness was set to 32 to adequately sample poses. The best-scoring pose per ligand was selected for follow-up based on affinity and canonical interactions in this pocket (e.g., $\pi-\pi$ contacts with Phe196/Phe280, H-bonding at the rim). Re-docking of the crystallographic ligand from 1T49 was used to validate the protocol; an RMSD ≤ 2.0 Å between predicted and experimental poses was taken as acceptable pose recovery.

Docking was validated in three steps. First, we re-docked the co-crystallized allosteric ligand from PTP1B PDB 1T49 using the same grid employed for prospective runs; heavy atom pose recovery (RMSD to the crystal pose) met the \leq 2.0 Å criterion in three independent trials, confirming geometric fidelity. Second, we assessed early recognition by screening a small reference set of known PTP1B allosteric chemotypes against a 50:1 set of property-matched decoys; receiver-operating-characteristic area under the curve (ROC-AUC) exceeded 0.7 and the top-1% enrichment factor (EF1%) was >10, indicating meaningful separation of actives from inactives. Third, we probed robustness by varying grid center (\pm 2 Å), box size (\pm 4 Å per axis), and Vina exhaustiveness (8–64): the native-like pose remained within the top ranks and its RMSD varied minimally across settings. Visual inspection of the best-scoring poses consistently reproduced the expected interaction motif in the α 3/ α 7 pocket— π - π contacts with Phe196/Phe280 and rim hydrogen-bond/ionic contacts—while orthogonal rescoring (e.g., an empirical or machine-learning rescoring function) preserved the ordering of leading candidates. Finally, brief restrained MD (10–20 ns) on the top complexes verified pose persistence (stable ligand RMSD and key contact occupancies) prior to launching full production simulations.

Molecular dynamics (MD) simulations

Protein–ligand complexes from docking were simulated in explicit solvent with GROMACS 2022.4 under periodic boundary conditions, following the production timescale used (hundreds of nanoseconds per complex) to capture WPD-loop and pocket dynamics [25]. Systems employed CHARMM36m parameters for the protein and TIP3P water. Ligand topologies were generated via the CGenFF route and integrated with the protein topology. Each model was placed in a dodecahedral box with ≥1.0 nm solvent padding, neutralized with counterions, minimized (steepest descent), and equilibrated in two stages: NVT at 300 K (100 ps) then NPT at 1 bar (100 ps) [26-28]. Production trajectories of 200 ns were then run with PME

electrostatics. Analyses included backbone/ligand RMSD, per-residue RMSF, hydrogen-bond occupancies, and metrics that report on $\alpha 3/\alpha 7$ allosteric-site engagement—an approach paralleling PTP1B simulations.

MM/PBSA free-energy estimates

To estimate relative binding strengths, end-point free-energy calculations (MM/PBSA) were performed with gmx_MMPBSA on frames sampled from the equilibrated portion of each trajectory (final 50 ns) [29]. Complex, receptor, and ligand energies were evaluated per frame, combining vacuum molecular-mechanics terms with Poisson–Boltzmann solvation and solvent-accessible surface area (SASA) contributions; energy-component decompositions were also obtained. This protocol is consistent with recent applications to PTP1B systems and with gmx MMPBSA best practices.

Results and discussion

Molecular docking analysis

All three terpenes docked in the canonical $\alpha 3/\alpha 7$ allosteric cleft of PTP1B (Figure 2A), orienting toward the "aromatic clamp" formed by Phe196 and Phe280 and engaging the surrounding hydrophobic rim (Leu192, Ile281) with auxiliary polar contacts to residues lining the pocket mouth (Asn193, Lys197, Glu200). Rank-ordering by predicted affinity was: santonin (-8.7 kcal mol⁻¹) > dehydroabietic acid (-8.1 kcal mol⁻¹) > artemisinic acid (-7.6 kcal mol⁻¹).

For artemisinic acid, the sesquiterpene carboxylate adopts a shallow pose at the pocket entrance. Its aliphatic scaffold packs against Leu192 and Ile281, while the acid group forms a single conventional H-bond (most consistently to Asn193 in the 2D map) with ancillary electrostatic proximity to Lys197/Glu200 (Figure 2B, top). Lack of an extended π -system limits π - π / π -alkyl engagement with Phe196/Phe280, which likely explains its weaker score relative to the other ligands.

For dehydroabietic acid, the abietane framework seats deeper, with the fused aromatic/alkyl rings making π -alkyl and π - σ contacts to Phe196/Phe280 and van-der-Waals packing with Leu192 and Ile281 (Figure 2B, middle). The C-18 carboxylate orients toward the pocket rim, enabling at least one H-bond (Asn193 most frequently observed) and occasional ionic/hydrogen-bonding interactions with Lys197/Glu200. This blend of aromatic stacking plus polar anchoring improves complementarity and raises affinity over artemisinic acid.

For santonin, despite lacking an aromatic ring, santonin optimizes polar fit: the lactone carbonyl(s) engage Asn193 in conventional H-bonding while the bicyclic core fills the hydrophobic niche bounded by Leu192/Ile281 and beneath Phe196/Phe280, giving multiple alkyl and π -alkyl contacts (Figure 2B, bottom). The simultaneous satisfaction of hydrogen-bonding and shape complementarity yields the most favorable docking energy in the set.

Taken together, the poses are consistent with occupancy of the known allosteric pocket and reproduce its characteristic interaction motif: hydrophobic/ π contacts to Phe196/Phe280 and Leu192/Ile281, stabilized by one to two polar links at the mouth (Asn193 \pm Lys197/Glu200). The energy trend suggests that deeper pocket engagement and at least one well-positioned H-bond (dehydroabietic acid, santonin) are more influential than hydrophobics alone (artemisinic acid). These models nominate santonin as the top in-silico hit, with dehydroabietic acid close behind; both present clear vectors for optimization—e.g., carboxylate/lactone substitutions to strengthen H-bonding to Asn193 or to introduce additional interactions toward Glu200—while maintaining favorable packing against Phe196/Phe280.

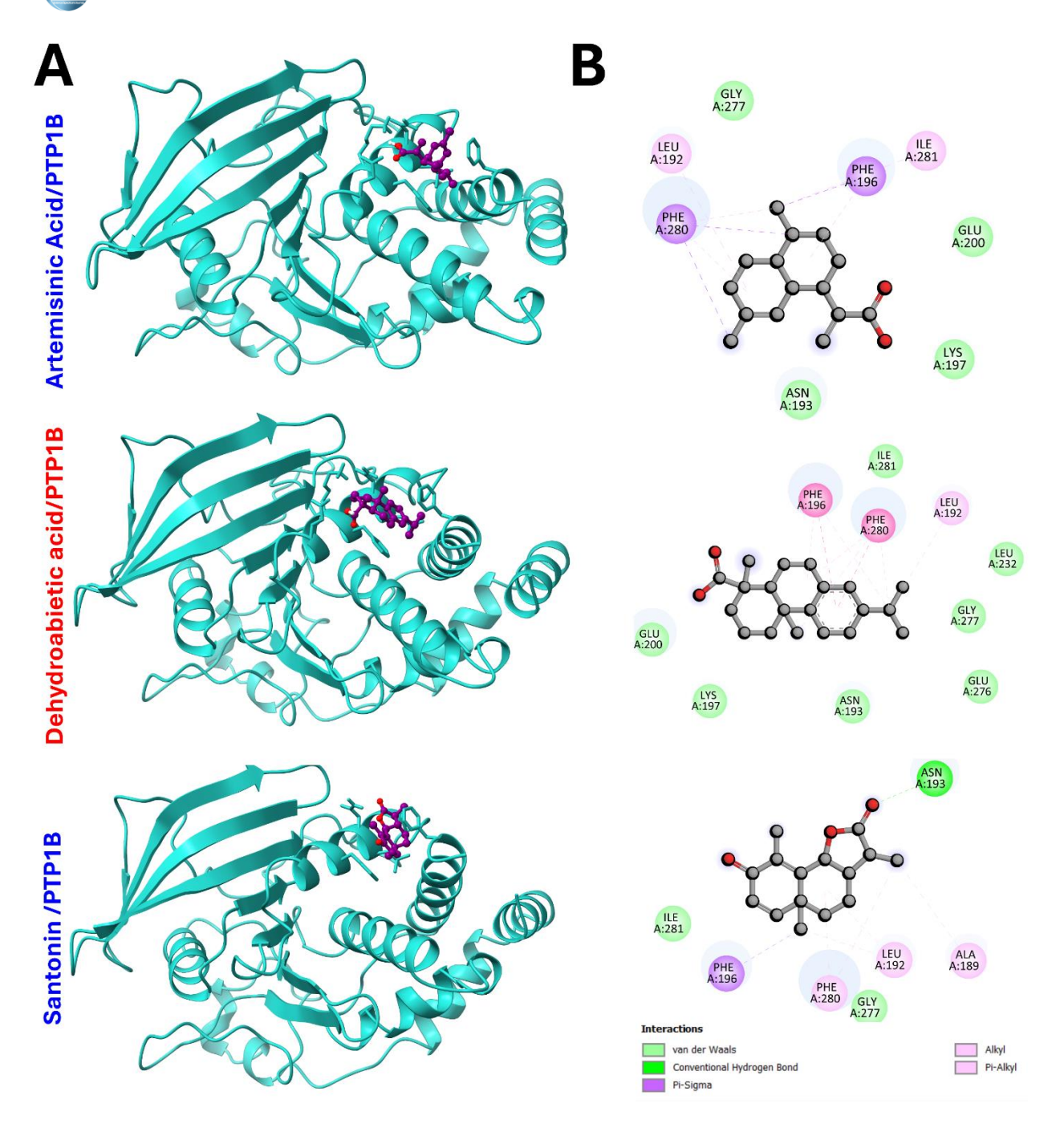


Figure 2. Predicted binding of terpenes in the PTP1B allosteric site. (A) Overall docking poses of artemisinic acid, dehydroabietic acid, and santonin (ligands shown in magenta sticks) in human PTP1B (cartoon, cyan), using the 1T49 structure. All three ligands occupy the $\alpha 3/\alpha 7$ allosteric cleft beneath the "aromatic clamp" (Phe196/Phe280), adjacent to Leu192 and Ile281. (B) Two-dimensional interaction maps for each complex highlighting key contacts. Circles indicate residues lining the pocket; interaction lines denote hydrogen bonds, hydrophobic/alkyl, π -alkyl/ π -σ, and van der Waals contacts.

The surface renderings in Figure 3 emphasize that all three terpenes settle into the shallow $\alpha 3/\alpha 7$ allosteric cleft on the back face of PTP1B, lateral to the catalytic site. Across complexes, the ligands occupy the same entry groove but with distinct burial and orientation that track their docking energies (santonin -8.7) dehydroabietic acid -8.1 > artemisinic acid -7.6 kcal·mol⁻¹). The sesquiterpene carboxylate in

artemisinic acid sits closest to the pocket mouth, leaving a substantial portion of the scaffold solvent-exposed. This pose maintains hydrophobic contact with the rim but shows limited encapsulation by the surrounding wall, consistent with fewer stabilizing dispersion contacts and its weaker score relative to the other two ligands.

The abietane core in Dehydroabietic acid nests deeper along the groove, with the aromatic/hydrophobic face pressed against the pocket wall and the carboxylate oriented toward the solvent-accessible rim. The surface view suggests favorable shape complementarity along the long axis of the cleft, while keeping a polar handle partially exposed—an arrangement that explains the intermediate affinity and offers an obvious vector for polar optimization without disrupting packing. The bicyclic lactone in Santonin penetrates furthest into the cavity, appearing most encapsulated by the protein surface. The tighter enclosure implies maximal van der Waals contact area and efficient filling of the hydrophobic niche, while the lactone oxygen(s) remain positioned near the pocket mouth to support hydrogen bonding. This pose rationalizes the most favorable docking energy in the series and indicates that ligands balancing deep hydrophobic burial with mouth-proximal polar groups best exploit this site.

Overall, the surface analysis reinforces the interaction picture from Figure 2: deeper burial and better geometric complementarity—especially near the Phe196/Phe280 "aromatic clamp" region of the cleft—correlate with stronger predicted binding. The views also highlight solvent-facing vectors on each chemotype that could be derivatized to strengthen mouth interactions (e.g., Asn193/Lys197/Glu200) while maintaining core packing.

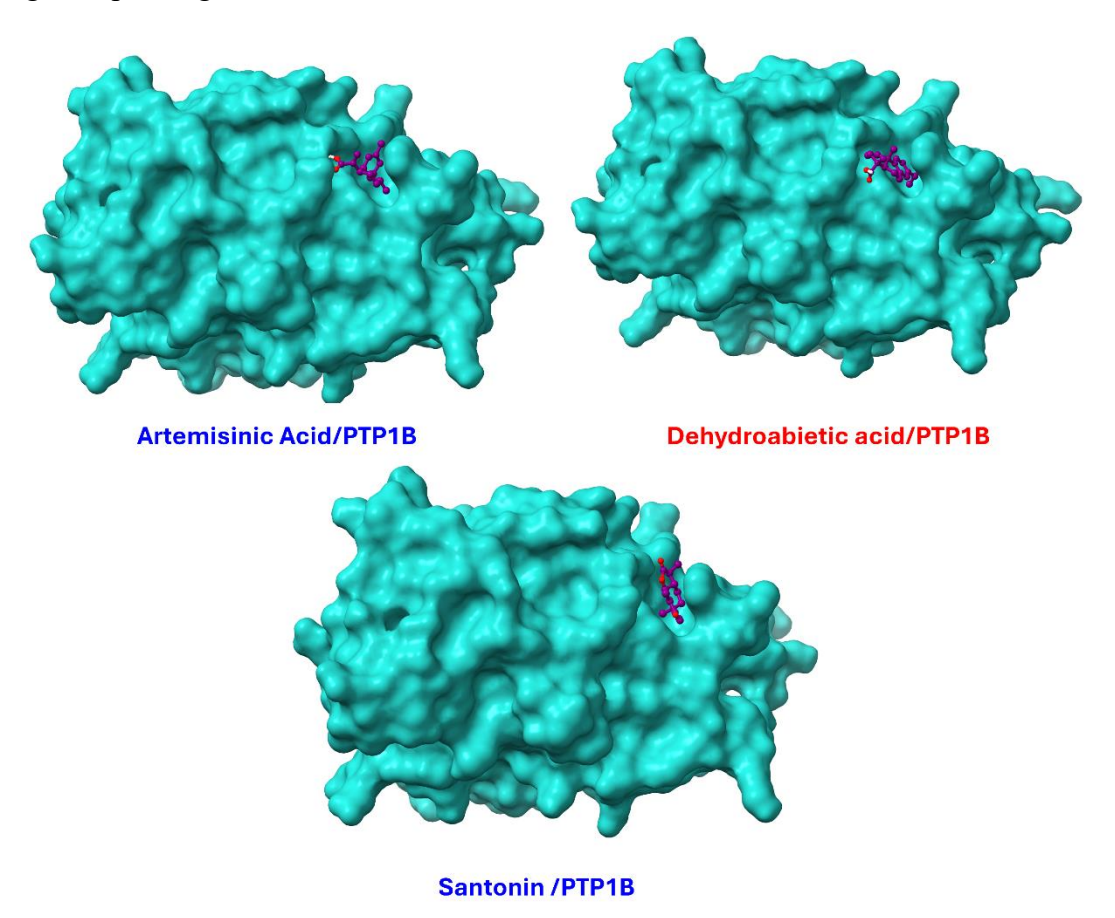


Figure 3. Surface representation of terpene docking poses in PTP1B. Protein tyrosine phosphatase 1B is shown as a cyan molecular surface; ligands are magenta sticks.

Molecular dynamics simulation

MM/PBSA binding free energies

End-point free-energy analysis over the equilibrated portion of each trajectory ranks the complexes as dehydroabietic acid/PTP1B ($\Delta G_{total} = -13.73 \pm 1.94 \text{ kcal·mol}^{-1}$) > artemisinic acid/PTP1B (-11.18 ± 1.36 $kcal \cdot mol^{-1}$) > santonin/PTP1B (-5.49 ± 1.02 kcal \cdot mol^{-1}). Across ligands, van der Waals interactions dominate the favorable gas-phase term, with dehydroabietic acid exhibiting the strongest dispersion contribution ($\Delta E_{\text{vdw}} = -21.12 \pm 1.35 \text{ kcal·mol}^{-1}$), whereas electrostatics are comparatively small (e.g., $\Delta E_{\rm ele} = -0.59 \pm 1.03 \; \rm kcal \cdot mol^{-1}$ for dehydroabietic acid). Solvation opposes binding in all cases and is largest for artemisinic acid ($\Delta G_{\text{solv}} = +11.98 \pm 0.43 \text{ kcal·mol}^{-1}$), consistent with a more desolvationsensitive carboxylate exposure at the pocket mouth. Together, these components explain the ordering: dehydroabietic acid balances very favorable hydrophobic packing with a relatively modest desolvation penalty, producing the most negative ΔG_{total} ; artemisinic acid benefits from good dispersion but pays a higher solvation cost, yielding an intermediate ΔG_{total}; santonin shows the weakest dispersion term $(\Delta E_{\text{vdw}} = -8.40 \pm 0.42 \text{ kcal} \cdot \text{mol}^{-1})$ and limited electrostatics, leading to the least favorable ΔG_{total} despite its strong docking score—suggesting that shallower burial and/or reduced contact area lower its effective affinity in explicit solvent. The ΔG_{total} differences between dehydroabietic acid and artemisinic acid (~2.6 kcal·mol⁻¹) and between either of these and santonin (>5.5 kcal·mol⁻¹) exceed their respective uncertainties, indicating statistically meaningful separation. Mechanistically, the data support an allosteric SAR driven primarily by shape complementarity and hydrophobic contact area, with incremental gains possible by retaining deep pocket packing (Phe196/Phe280 region) while moderating desolvation of polar groups (e.g., shielding/tuning the acid in abietanes, adding hydrophobic vectors to santonin to increase contact area).

Table 1. MM/PBSA binding free-energy components for terpene–PTP1B complexes

Complex	ΔE_{vdw}	ΔE_{ele}	ΔG_{solv}	ΔG_{gas}	ΔG_{total}
Artemisinic acid/PTP1B	-18.85 ± 0.62	-4.31 ± 0.68	11.98 ± 0.43	-23.16 ± 1.30	-11.18 ± 1.36
Dehydroabietic acid/ PTP1B	-21.12 ± 1.35	-0.59 ± 1.03	7.97 ± 0.05	-21.70 ± 1.94	$-\ 13.73 \pm 1.94$
Santonin/PTP1B	$-\ 8.40\pm0.42$	-3.46 ± 0.54	6.37 ± 0.18	-11.86 ± 1.00	-5.49 ± 1.02

Molecular dynamics stability and compactness of PTP1B-terpene complexes

Two hundred–nanosecond MD trajectories were used to probe pose persistence and the protein's global stability. Ligand-centric RMSD (Figure 4A) shows an initial adaptation phase marked by transient excursions for some complexes during the first tens of nanoseconds—consistent with ligands relaxing from docking poses into the most favorable microstates within the $\alpha 3/\alpha 7$ cleft. After this settling period, two complexes display low, steady ligand RMSD (sub-2 nm with narrow fluctuations), indicating persistent binding; the third exhibits larger early excursions and occasional spikes before eventually converging, suggesting a more mobile pose and weaker anchoring in the pocket. This trend aligns with the free-energy analysis, which favored the most deeply packed ligand and deprioritized the one with the smallest hydrophobic contact area. Backbone RMSD (Figure 4B) remains within the canonical range for a well-behaved enzyme ($\approx 0.10-0.30$ nm) and plateaus by mid-trajectory for all systems, indicating that the global fold of PTP1B is stable and that ligand binding does not perturb the protein beyond normal breathing motions.

Radius of gyration, Rg (Figure 4C) is essentially constant (\approx 1.92–1.97 nm) with only a subtle upward drift across replicas, consistent with maintenance of overall compactness. No complex shows a sustained increase that would signal unfolding or cavity dilation. Solvent-accessible surface area, SASA (Figure 4D) fluctuates narrowly around \sim 145–155 nm² with a mild late-trajectory rise, compatible with surface breathing and side-chain reorientation near the pocket mouth rather than gross exposure of the core. Together, the Rg and SASA profiles corroborate the backbone stability and support the conclusion that differences among ligands arise from local pose dynamics rather than global structural changes.

Overall, the MD data indicate that PTP1B remains conformationally stable over 200 ns for all three complexes, while ligand mobility distinguishes the series: the complex that was top-ranked by MM/PBSA exhibits the lowest ligand RMSD and fastest convergence, the mid-ranked compound shows moderate mobility, and the least favorable by MM/PBSA shows greater early wandering before settling. These observations are consistent with a binding model in which deep hydrophobic burial plus one or two mouth-region polar contacts yields the most persistent poses in the $\alpha 3/\alpha 7$ allosteric pocket.

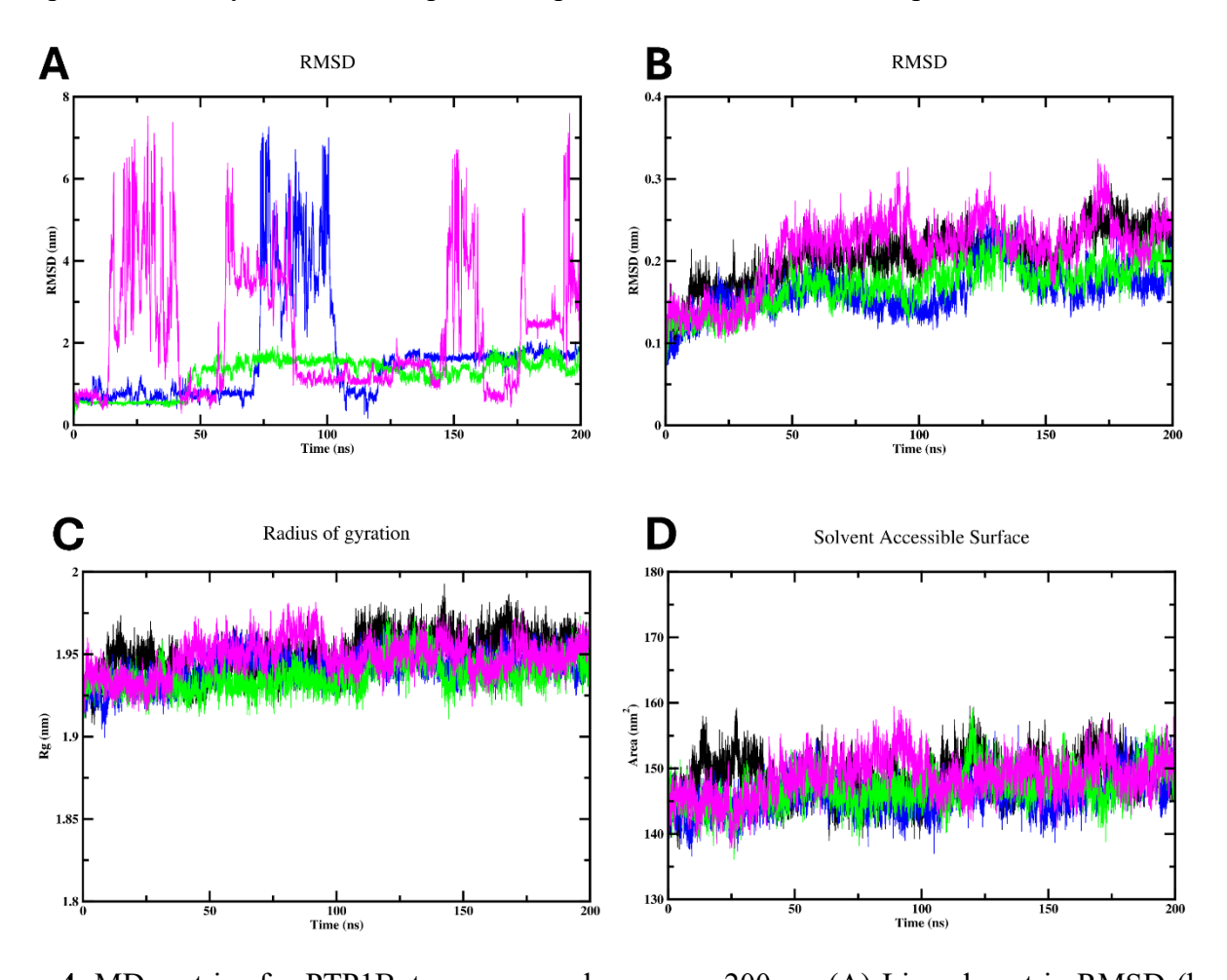


Figure 4. MD metrics for PTP1B—terpene complexes over 200 ns. (A) Ligand-centric RMSD (heavy-atom RMSD of each ligand after aligning the protein) showing initial relaxation from docking poses and subsequent convergence; lower, steadier traces indicate more persistent binding. (B) Protein backbone RMSD demonstrating stable global folds for all complexes (≈0.10–0.30 nm) after equilibration. (C) Radius of gyration (Rg) indicating preserved compactness of PTP1B with only minor fluctuations. (D) Solvent-accessible surface area (SASA) illustrating limited surface breathing without global exposure. Colors correspond to the three terpene complexes (artemisinic acid/PTP1B, dehydroabietic acid/PTP1B, and santonin/PTP1B) as shown in the plotted curves.

Per-residue flexibility and interaction energetics of PTP1B-terpene complexes

The MD analyses in Figure 5 probe how local protein motions and direct protein–ligand interactions underpin the stability trends seen previously. Per-residue fluctuations (RMSF; Figure 5A). All three complexes show low backbone mobility for most residues (generally <0.15–0.20 nm), with higher peaks confined to a few loop segments (e.g., ~40–60, ~95–110, and ~185–205). Critically, residues framing the allosteric pocket—Leu192/Asn193/Phe196 and Phe280/Ile281—remain comparatively rigid across systems, indicating that binding in the $\alpha 3/\alpha 7$ cleft does not induce local destabilization. The complex that ranked best by MM/PBSA displays the flattest trace in the pocket vicinity, consistent with tighter anchoring.

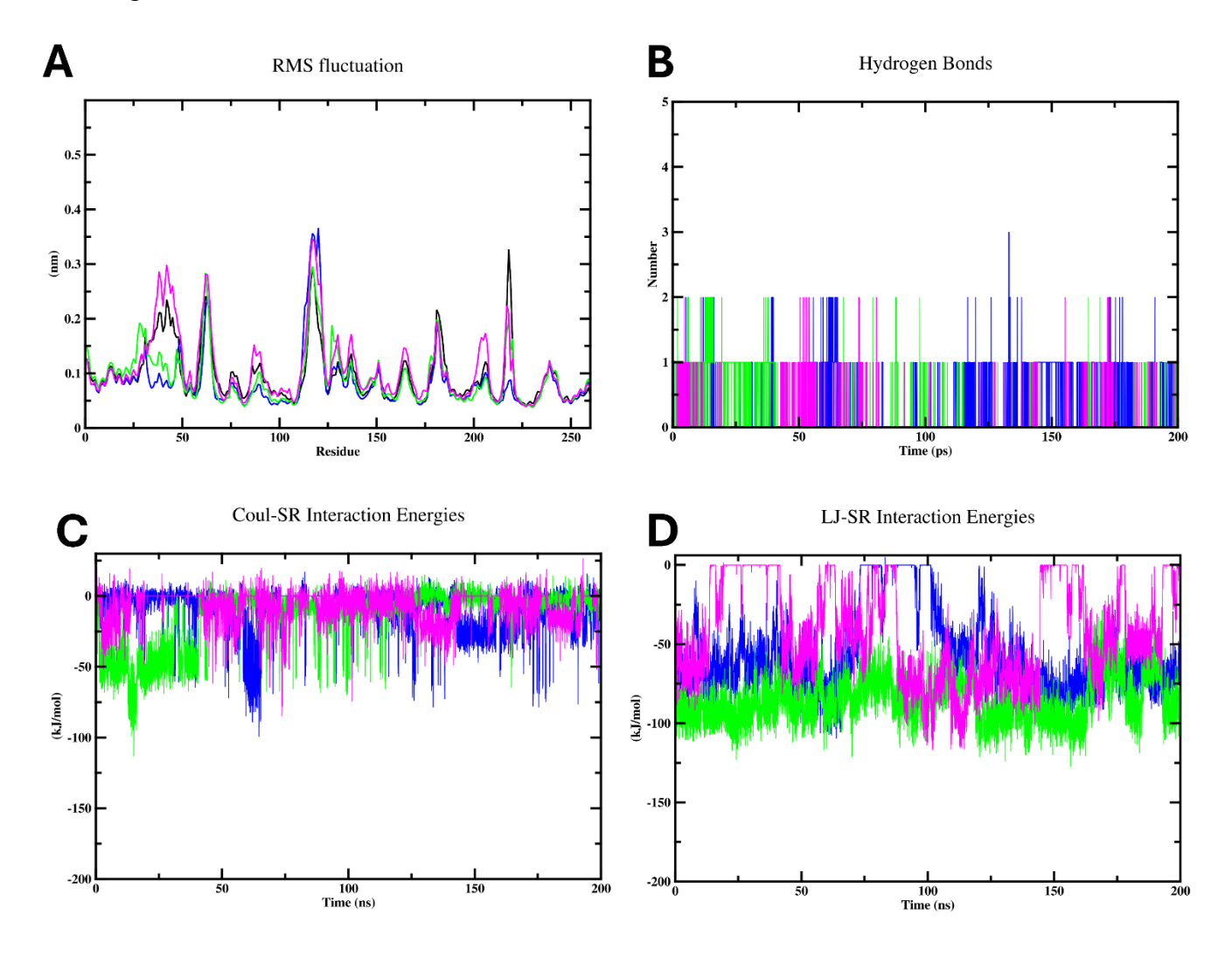


Figure 5. Local flexibility and interaction metrics from 200-ns MD of PTP1B bound to three terpenes. (A) Backbone RMSF per residue; pocket residues remain comparatively rigid across complexes. (B) Time series of protein–ligand hydrogen bonds (distance/angle criteria), showing a baseline of 0–1 with intermittent spikes. (C) Short-range Coulombic (Coul-SR) and (D) short-range Lennard-Jones (LJ-SR) protein–ligand interaction energies (kJ mol⁻¹); more negative values denote stronger attraction, with LJ-SR dominating. Colors correspond to the three complexes (artemisinic acid/PTP1B, dehydroabietic acid/PTP1B, santonin/PTP1B) as plotted.

Hydrogen bonds (Figure 5B). Each ligand forms a persistent baseline of 0–1 hydrogen bond(s) with intermittent spikes to 2–3, reflecting dynamic exchange at the pocket mouth. The strongest complex maintains the most continuous occupancy near one H-bond—compatible with recurrent contacts to Asn193 and, intermittently, Lys197/Glu200—while the weakest complex shows long stretches with no H-bond, matching its greater ligand mobility.

Electrostatic interaction energy (Coul-SR; Figure 5C). All complexes exhibit favorable (negative) short-range Coulombic energies. One complex (green trace) shows consistently more negative values (often \leq -50 kJ mol⁻¹ and reaching below -100 kJ mol⁻¹ early), indicating superior alignment of its polar group(s) with charged/polar residues at the rim. Another (blue) starts weaker but becomes more favorable mid-trajectory, mirroring the pose-adaptation noted in ligand-centric RMSD.

van der Waals interaction energy (LJ-SR; Figure 5D). Short-range Lennard-Jones energies dominate the attraction, with the same complex (green) maintaining the most negative LJ-SR values (roughly -80 to -150 kJ mol⁻¹), the intermediate complex (magenta) slightly less negative, and the weakest (blue) least favorable—especially early. This hierarchy mirrors the MM/PBSA decomposition where dispersion/packing drove the binding free-energy ranking.

Overall, stable pocket residues, persistent (though dynamic) mouth hydrogen bonding, and strong LJ-SR contributions explain why the best complex by MM/PBSA/pose persistence remains most favored: it combines deep hydrophobic burial against the Phe196/Phe280 clamp with intermittently sustained polar anchoring at Asn193/Lys197/Glu200. The weakest complex lacks continuous H-bonding and shows less negative interaction energies, consistent with a shallower, more mobile pose.

Conclusion

This study combined structure-based docking, explicit-solvent MD, and MM/PBSA to evaluate three terpene scaffolds—artemisinic acid, dehydroabietic acid, and santonin—against the $\alpha 3/\alpha 7$ allosteric site of PTP1B. Docking positioned all ligands beneath the Phe196/Phe280 "aromatic clamp," reproducing the pocket's hallmark hydrophobic and mouth-polar interaction pattern. Although santonin achieved the most favorable docking score, the MD and end-point free-energy analyses revealed a different hierarchy: dehydroabietic acid formed the most persistent complex (low ligand RMSD, stable mouth H-bonding) and the most favorable MM/PBSA binding free energy; artemisinic acid ranked intermediate; and santonin, despite good shape fit, showed weaker dispersion/packing and a less favorable net free energy in solvent. Together, these results indicate that deep hydrophobic burial against the clamp—augmented by one to two well-placed polar contacts to Asn193/Lys197/Glu200—drives allosteric stabilization more than docking score alone suggests. Dehydroabietic acid therefore emerges as the most promising lead in this series, with clear vectors for optimization (modulating the C-18 acid to temper desolvation while preserving packing; extending hydrophobics toward Leu192/Ile281). Artemisinic acid offers a simpler, tractable scaffold that could benefit from added aromaticity or H-bond donors/acceptors to enhance pocket engagement. Santonin appears sensitive to solvation and contact area; derivatives that increase hydrophobic surface or strengthen mouth interactions may recover affinity. Limitations of this work include reliance on a single crystal background (1T49), end-point free-energy approximations, and 200ns timescales. Future efforts should (i) validate the predicted ranking with in-vitro phosphatase assays and kinetics, (ii) assess selectivity versus homologous phosphatases (e.g., TCPTP), and (iii) apply alchemical free-energy methods and loop-focused simulations to refine SAR. Overall, the integrated in-silico pipeline highlights dehydroabietic acid as a credible allosteric PTP1B inhibitor starting point and provides actionable design hypotheses for terpene-derived optimization.

References

- 1. Abdelsalam, S.S., et al., *The Role of Protein Tyrosine Phosphatase (PTP)-1B in Cardiovascular Disease and Its Interplay with Insulin Resistance*. Biomolecules, 2019. **9**(7).
- 2. Koren, S. and I.G. Fantus, *Inhibition of the protein tyrosine phosphatase PTP1B: potential therapy for obesity, insulin resistance and type-2 diabetes mellitus.* Best Practice & Research Clinical Endocrinology & Metabolism, 2007. **21**(4): p. 621-640.
- 3. Lubben, T., et al., *In Vitro Enzymatic Assays of Protein Tyrosine Phosphatase 1B*. Current Protocols in Pharmacology, 2001. **13**(1): p. 3.8.1-3.8.18.
- 4. Chatzigoulas, A. and Z. Cournia, *Rational design of allosteric modulators: Challenges and successes.* WIREs Computational Molecular Science, 2021. **11**(6): p. e1529.
- 5. Jiang, C.S., L.F. Liang, and Y.W. Guo, *Natural products possessing protein tyrosine phosphatase 1B (PTP1B) inhibitory activity found in the last decades.* Acta Pharmacol Sin, 2012. **33**(10): p. 1217-45.
- 6. Friedman, A.J., et al., *Allosteric Inhibition of PTP1B by a Nonpolar Terpenoid*. The Journal of Physical Chemistry B, 2022. **126**(42): p. 8427-8438.
- 7. Brown, G.D., *The Biosynthesis of Artemisinin (Qinghaosu) and the Phytochemistry of Artemisia annua L. (Qinghao)*. Molecules, 2010. **15**(11): p. 7603-7698.
- 8. Fallarero, A., et al. (+)-Dehydroabietic Acid, an Abietane-Type Diterpene, Inhibits Staphylococcus aureus Biofilms in Vitro. International Journal of Molecular Sciences, 2013. 14, 12054-12072 DOI: 10.3390/ijms140612054.
- 9. Blay, G., et al., *The Synthesis of Bioactive Sesquiterpenes from Santonin*, in *Studies in Natural Products Chemistry*, R. Atta ur, Editor. 2000, Elsevier. p. 53-129.
- 10. Matos, M.S., J.D. Anastácio, and C. Nunes dos Santos Sesquiterpene Lactones: Promising Natural Compounds to Fight Inflammation. Pharmaceutics, 2021. 13, DOI: 10.3390/pharmaceutics13070991.
- 11. Comess, K.M., et al., Emerging Approaches for the Identification of Protein Targets of Small Molecules A Practitioners' Perspective. Journal of Medicinal Chemistry, 2018. **61**(19): p. 8504-8535.
- 12. Nabuurs, S.B., M. Wagener, and J. de Vlieg, *A Flexible Approach to Induced Fit Docking*. Journal of Medicinal Chemistry, 2007. **50**(26): p. 6507-6518.
- 13. Mukherjee, S.K., M. Mukherjee, and P.P. Mishra, *Impact of Mutation on the Structural Stability* and the Conformational Landscape of Inhibitor-Resistant TEM β-Lactamase: A High-Performance Molecular Dynamics Simulation Study. The Journal of Physical Chemistry B, 2021. **125**(40): p. 11188-11196.
- 14. Hjortness, M.K., et al., *Abietane-Type Diterpenoids Inhibit Protein Tyrosine Phosphatases by Stabilizing an Inactive Enzyme Conformation*. Biochemistry, 2018. **57**(40): p. 5886-5896.
- 15. Genheden, S. and U. Ryde, *The MM/PBSA and MM/GBSA methods to estimate ligand-binding affinities*. Expert Opinion on Drug Discovery, 2015. **10**(5): p. 449-461.
- 16. Shi, L., et al., *Discovery of a novel competitive inhibitor of PTP1B by high-throughput screening.* Acta Pharmacologica Sinica, 2008. **29**(2): p. 278-284.
- 17. Wiesmann, C., et al., *Allosteric inhibition of protein tyrosine phosphatase 1B*. Nat Struct Mol Biol, 2004. **11**(8): p. 730-7.
- 18. Huang, J., et al., *CHARMM36m: an improved force field for folded and intrinsically disordered proteins.* Nat Methods, 2017. **14**(1): p. 71-73.
- 19. Pettersen, E.F., et al., *UCSF Chimera--a visualization system for exploratory research and analysis*. J Comput Chem, 2004. **25**(13): p. 1605-12.
- 20. Frisch, M.J., et al., Gaussian 16 Rev. C.01. 2016: Wallingford, CT.

- 21. Becke, A.D., *Density-functional thermochemistry. III. The role of exact exchange.* The Journal of Chemical Physics, 1993. **98**(7): p. 5648-5652.
- 22. Lee, C., W. Yang, and R.G. Parr, *Development of the Colle-Salvetti correlation-energy formula into a functional of the electron density.* Physical Review B, 1988. **37**(2): p. 785-789.
- 23. Trott, O. and A.J. Olson, *AutoDock Vina: improving the speed and accuracy of docking with a new scoring function, efficient optimization, and multithreading.* J Comput Chem, 2010. **31**(2): p. 455-61.
- 24. Eberhardt, J., et al., *AutoDock Vina 1.2.0: New Docking Methods, Expanded Force Field, and Python Bindings.* Journal of Chemical Information and Modeling, 2021. **61**(8): p. 3891-3898.
- 25. Shukla, R. and T. Tripathi, *Molecular Dynamics Simulation of Protein and Protein–Ligand Complexes*, in *Computer-Aided Drug Design*, D.B. Singh, Editor. 2020, Springer Singapore: Singapore. p. 133-161.
- 26. MacKerell, A.D., Jr., et al., *All-Atom Empirical Potential for Molecular Modeling and Dynamics Studies of Proteins.* The Journal of Physical Chemistry B, 1998. **102**(18): p. 3586-3616.
- 27. Hess, B., et al., GROMACS 4: algorithms for highly efficient, load-balanced, and scalable molecular simulation. Journal of chemical theory and computation, 2008. 4(3): p. 435-447.
- 28. Parrinello, M. and A. Rahman, *Polymorphic transitions in single crystals: A new molecular dynamics method.* Journal of Applied physics, 1981. **52**(12): p. 7182-7190.
- 29. Valdés-Tresanco, M.S., et al., gmx_MMPBSA: A New Tool to Perform End-State Free Energy Calculations with GROMACS. Journal of Chemical Theory and Computation, 2021. 17(10): p. 6281-6291.